Nanopatterning of Surfaces with Monometallic and Heterobimetallic 1D Coordination Polymers: A Molecular Tectonics Approach at the Solid/Liquid Interface

Mohamed El Garah,[†] Nicolas Marets,[§] Matteo Mauro,[‡,||] Alessandro Aliprandi,[‡] Sara Bonacchi,[†] Luisa De Cola,[‡] Artur Ciesielski,*[,†] Véronique Bulach,*[,§] Mir Wais Hosseini,*[,§] and Paolo Samorì*[,†]

[†]Laboratoire de Nanochimie and [‡]Laboratoire de Chimie et des Biomatériaux Supramoléculaires, Institut de Science et d'Ingénierie Supramoléculaires (ISIS) and International Center for Frontier Research in Chemistry (icFRC), Université de Strasbourg and Centre National de la Recherche Scientifique (CNRS), 8 allée Gaspard Monge, 67000 Strasbourg, France

[§]Laboratoire de Tectonique Moléculaire, UMR UdS-CNRS 7140 and icFRC, Institut Le Bel, Université de Strasbourg, 4 rue Blaise Pascal, CS 90032, 67081 Strasbourg, France

[||]Institut d'Etudes Avancées (USIAS), Université de Strasbourg, 5 allée du Général Rouvillois, 67083 Strasbourg, France

S *Supporting Information*

ABSTRACT: The self-assembly of multiple molecular components into complex supramolecular architectures is ubiquitous in nature and constitutes one of the most powerful strategies to fabricate multifunctional nanomaterials making use of the *bottom-up* approach. When spatial confinement in two dimensions on a solid substrate is employed, this approach can be exploited to generate periodically ordered structures

from suitably designed molecular tectons. In this study we demonstrate that physisorbed directional periodic arrays of monometallic or heterobimetallic coordination polymers can be generated on a highly oriented pyrolitic graphite surface by combinations of a suitably designed directional organic tecton or metallatecton based on a porphyrin or nickel(II) metalloporphyrin backbone bearing both a pyridyl unit and a terpyridyl unit acting as coordinating sites for $CoCl_2$. The periodic architectures were visualized at the solid/liquid interface with a submolecular resolution by scanning tunneling microscopy and corroborated by combined density functional and time-dependent density functional theory calculations. The capacity to nanopattern the surface for the first time with two distinct metallic centers exhibiting different electronic and optical properties is a key step toward the bottom-up construction of robust multicomponent and, thus, multifunctional molecular nanostructures and nanodevices.
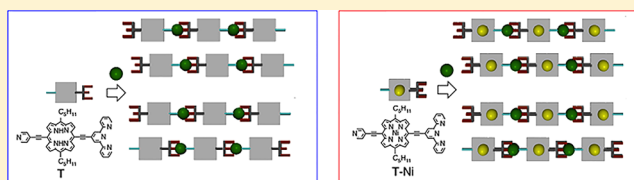
1. INTRODUCTION

Molecular tectonics is a field of research exploiting the principles of supramolecular chemistry to generate extended 1D, 2D, or 3D periodic architectures called molecular networks.[1] This approach relies on combinations of complementary building blocks or tectons bearing within their structures complementary specific interaction sites leading to the formation of recognition patterns. Upon repetition of the assembly processes, the recognition patterns become structural nodes of the network. Among many possible intermolecular interactions, coordination bonding, taking place between organic coordinating tectons and metal centers or complexes, leads to coordination polymers or networks.[2] The latter in the crystalline phase has been the subject of intense studies because of the unique properties of the tailored architecture, offering potential for numerous technological applications. Although since the groundbreaking contribution by R. Robson et al. in 1991[3] many examples of coordination networks or metal–organic frameworks (MOFs) have been reported,[4] the design of heterometallic extended architectures,[5] and of directional assemblies,[6] still represents a great challenge.

The development of scanning tunneling microscopy (STM) enabling the subnanometer-resolved visualization of molecules at surfaces triggered the emergence of 2D crystal engineering at surfaces and interfaces.[7] The latter field is instrumental to nanoscience and nanotechnology since controlling surface patterning with subnanometer precision and both short- and long-range order is of prime importance for fundamental studies, e.g., exploring collective properties at the nanoscale, as well as for more technologically relevant applications such as fabrication of multifunctional nanodevices such as switchable transistors.[8] For example, monomolecular transistors based on terpyridyl–cobalt–terpyridyl complexes,[9] as well as dynamic chemical devices undergoing reversible extension/contraction through a pH-triggered complexation of Pb ions,[10] have been reported.

STM has been proven to be a powerful tool not only to explore molecules at surfaces and interfaces with a subnanometer resolution,[11] but also to unravel numerous physico-

Scheme 1. Synthesis of Tectons T and T−Ni[a]
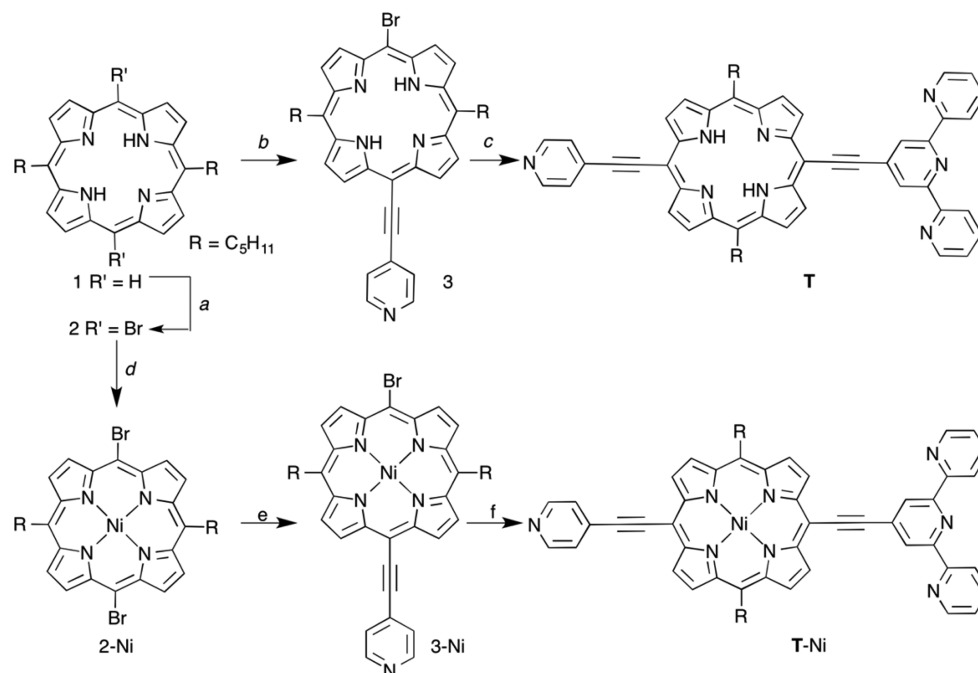
[a]Reagents: (a) NBS, (b) AsPh$_3$, Pd$_2$(dba)$_3$, 4-ethynylpyridine, (c) AsPh$_3$, Pd$_2$(dba)$_3$, 4-ethynylterpyridine, (d) Ni(OAc)$_2$·4H$_2$O, (e) PdCl$_2$(PPh$_3$)$_2$, CuI, 4-ethynylpyridine, (f) PdCl$_2$(PPh$_3$)$_2$, CuI, 4-ethynylterpyridine.

chemical properties,[12] including the electronic density states of the molecules on the surfaces.[13] Furthermore, over the past decade, STM appeared as the tool of choice to explore at the nanometric scale intermolecular interactions in 1D/2D supramolecular architectures created by means of the *bottom-up* approach. STM has also been used to study 2D coordination networks based on combinations of metal centers with organic ligands bearing carboxylate,[14] carbonitrile,[15] pyridine,[16] and cyano[17] groups. However, the self-assembled structures at the solid/liquid interfaces reported so far are homometallic in nature, and to the best of our knowledge, no examples of a 1D heterometallic coordinated network have been reported to date.

Porphyrin derivatives exhibit peculiar optoelectronic properties rendering them key components for various applications including solar cells[13b,18] and photocatalysis.[19] Furthermore, the porphyrin scaffold is a candidate of choice for the design of organic coordinating tectons owing to their unique electronic structure, the propensity of their tetraaza core to bind metal centers, and their functionalization possibilities at both *meso* and *β*-pyrrolic positions. While numerous examples of 1D homometallic coordination arrays have been reported,[20] to the best of our knowledge, there are no examples describing heterometallic assemblies.[21]

In this study we extend the molecular tectonics approach to surface patterning by forming 1D directional homo- or heterometallic 1D coordination networks on a highly ordered pyrolytic graphite (HOPG) surface at the solid/liquid interface. The self-assembly of the porphyrin **T** and its Ni complex **T−Ni**, as the tecton and metallatecton, respectively (Scheme 1), with CoCl$_2$ as the connecting metallic center was investigated; in particular, the formation of designed monometallic Co(II) and heterobimetallic Co(II)−Ni(II) 1D networks was monitored in situ by STM. Experimental STM results have been corroborated theoretically by denisty functional theory (DFT),

providing insight into the electronic properties of tectons **T** and **T−Ni**.

2. RESULTS AND DISCUSSION

2.1. Design and Synthesis of T and T−Ni Tectons. On the basis of our previous studies on the formation of porphyrin-based coordination networks in the crystalline phase,[5i,22] tecton **T** and metallatecton **T−Ni** were designed (Scheme 1). Compound **T** is an acentric tecton bearing two different coordinating poles, a pyridyl unit and a 2,2′:6′,2″-terpyridyl unit, located at opposite *trans meso* positions on the porphyrin backbone, thereby acting as monodentate and tridentate coordinating moieties. Both poles are connected to the porphyrin through a conformationally rigid ethynyl spacer. The latter was chosen to guarantee the coplanarity of the coordinating poles and the porphyrin main plane and thus to increase the interactions with the HOPG surface. The remaining other two *trans meso* positions were decorated with two pentyl side chains to promote the solubility of the tecton **T** in organic solvents and to further enhance its affinity for the surface.

Overall, compound **T** may be considered as a tecton offering three coordinating sites composed of the central tetraaza core, the monodentate pyridyl, and the tridentate terpyridyl peripheral moieties. Owing to the high affinity of the central part of the tecton for the Ni(II) cation, the metalated porphyrin **T−Ni** was specifically generated. The latter, bearing two peripheral coordinating poles, may be used as a metallatecton for the formation of heterobimetallic architectures.

Although *meso*-substituted porphyrin derivatives bearing one or two terpyridyl or ethynylterpyridyl groups have been described,[23] the synthesis of unsymmetrically *meso*-substituted porphyrin derivatives bearing an ethynylterpyridyl unit and a pyridyl units has never been reported.

Tecton **T** was obtained by a multistep procedure starting from the 5,15-dipentylporphyrin **1** (Scheme 1).[24] The quantitative bromination of the remaining unsubstituted *meso* positions in the intermediate **1** using 2.1 equiv of *N*-bromosuccinimide (NBS) in CHCl$_3$ yielded the porphyrin **2**.[25] The introduction of the ethynylpyridine affording compound **3** in 36% yield was achieved using a copper-free Sonogashira coupling reaction.[26] In the last step, ethynylterpyridine was reacted with compound **3** in the presence of Pd$_2$(dba)$_3$ and AsPh$_3$, yielding the desired tecton **T** in 52% yield (see the Supporting Information for details).

The metallatecton **T**−**Ni** was obtained using a route similar to the one used for the synthesis of **T**. Owing to the presence of pyridyl or terpyridyl moieties, to avoid any interference between the tetraaza moiety and the two peripheral coordinating units, a Ni(II) cation was introduced within the central core of the porphyrin using the free porphyrin **2**. The **2**−**Ni** intermediate was obtained quantitatively upon metalation of **2** by Ni(OAc)$_2$ in DMF. The Sonogashira coupling between **2**−**Ni** and ethynylpyridine afforded **4**−**Ni** in 33% yield. Due to the presence of the Ni(II) within the center of the porphyrin, the Sonogashira coupling reaction was achieved using classical conditions in the presence of PdCl$_2$(PPh$_3$)$_2$ and CuI.[27] Finally, the desired metallatecton **T**−**Ni** was prepared in 40% yield under similar conditions upon coupling **4**−**Ni** and ethynylterpyridine.

2.2. DFT Calculations. to gain insight into the electronic properties of tectons **T** and **T**−**Ni**, DFT calculations were carried out at their electronic ground state. In particular, we employed the exchange-correlation hybrid functional B3LYP at the 6-31g(d,p) and LANL2DZ level of theory in the gas phase since it is known to be adequate for computational investigations of porphyrin-based systems.[28] Furthermore, to better simulate the conformation adopted by the two investigated tectons once physisorbed onto the HOPG surface, geometrical constraints were imposed on the dihedral angle (ϕ = 0°) of the two lateral pyridyl moieties of the terpyridyl fragment for all the compounds to keep the terpyridyl moiety of the molecules flat.

First, compound **T** has been optimized at the B3LYP/6-31g level of theory imposing the C_s point group symmetry, where the σ-symmetry plane contains the molecule. Vibrational frequency analysis on the stationary point revealed the presence of two imaginary frequencies of 15i and 11i corresponding to the rotation of the alkyl chains present on two *meso* positions. Distortion of the molecule along such imaginary modes and further optimization gave a molecular geometry with a C_1 symmetry in which the two pentyl chains point out of the molecular plane defined by the terpyridyl−porphyrin−pyridyl fragment toward the two opposite directions. Such a C_1 geometry is 15.6 kcal mol^{-1} more stable than the C_s geometry, and was found to be a true minimum since no imaginary mode was computed. Nonetheless, starting from the C_s- and C_1-optimized geometries at the 6-31g level and employing either the 6-31g(d) or the 6-31g(d,p) basis set, the optimization gave very similar geometries with respect to the nonpolarized basis set, where the C_1 geometry was found to be 15.7 and 15.5 kcal mol^{-1}, respectively, more stable than the C_s geometry. The C_s and C_1 structures computed at the 6-31g(d,p) level are displayed in Figure S5 (Supporting Information).

In a similar manner, three stationary points have been found for **T**−**Ni** optimized at the B3LYP/6-31g level, one with C_1 symmetry and two with C_s symmetry. As for the latter cases, the

C_s configuration in which the symmetry plane contains the molecule was found to be a saddle point with imaginary frequencies of 20i, 19i, and 14i corresponding to the ruffling of the porphyrin core. Such a C_s configuration, called C_s(a) in Figure S6 of the Supporting Information, was found to lie 17.4 kcal mol^{-1} (whereas 17.1 and 16.9 kcal mol^{-1} for 6-31g(d) or 6-31g(d,p), respectively) higher in energy than the other two conformations. On the other hand, the C_s geometry in which the symmetry plane bisects the molecule along the terpyridyl−porphyrine−pyridyl axis, namely, C_s(b) was found to be a true minimum, being energetically and geometrically very close (i.e., only 0.01 kcal mol^{-1} higher) to the C_1 geometry (Figure S6).[29] Such a ruffled geometry adopted by the porphyrin core in tecton **T**−**Ni** is in agreement with already reported data for nickel(II) porphyrin *meso*-substituted with alkyl groups.[30]

We can anticipate that on the basis of the STM images hereafter discussed (vide infra), we believe that the geometry of the molecules **T** and **T**−**Ni** on the HOPG surface could not correspond to the C_1 and C_s energy minima found in the gas phase and discussed above, in particular as far as the alkyl chains and planarity of the molecule are concerned. This is indeed due to the fact that different interactions between the molecule and surface as well as the molecule and solvent, such as π−π and van der Waals, play important roles in inducing a flattening of the molecule and of the side alkyl chains to maximize the interaction energy.[31] Because of these reasons, and to reduce the conformational space as well, we carried out geometrical optimization on the molecules **T** and **T**−**Ni** where pentyl pendant chains have been replaced by shorter methyl groups, namely, **T$_{Me}$** and **T$_{Me}$**−**Ni**, since they are expected to play a similar role in the electronic and optical properties of the molecules under investigation.

Geometrical optimization of **T$_{Me}$** at the B3LYP/6-31g(d,p) level yielded a symmetric (C_s) minimum where the σ-symmetry plane contains the molecule (see the Supporting Information for further details). Such a conformation exhibits C$_{\alpha,pyrrole}$−C$_{meso}$−C'$_{\alpha,pyrrole}$ angles of 124.4° and 126.2°, where C$_{\alpha,pyrrole}$ is the carbon atom of the pyrrolic moiety directly bound to the *meso* carbon (C$_{meso}$). On the other hand, optimized **T$_{Me}$**−**Ni** displays a C_s geometry in which the symmetry plane bisects the molecule along the terpyridyl−porphyrine−pyridyl (C$_{meso,tpy}$−Ni−C'$_{meso,tpy}$) axis. The C_s-symmetric **T$_{Me}$**−**Ni** adopts a slightly raffled conformation with C$_{\alpha,pyrrole}$−C$_{meso}$−C'$_{\alpha,pyrrole}$ angles of 121.1° and 121.8°, and a C$_{meso,Me}$−Ni−C'$_{meso,Me}$ angle of 161.5°, where C$_{meso,Me}$ and C'$_{meso,Me}$ are the two opposite *meso* carbon atoms bound to the methyl groups. The DFT-optimized geometries of **T**−**Ni** and **T$_{Me}$**−**Ni** are in agreement with already reported structures, and they are shown in Figure 1a.[30] A more detailed discussion about geometry optimization and selection criteria is given in section 2.1 of the Supporting Information.

Overall, the frontier orbital analysis of the computed porphyrins **T$_{Me}$** and **T$_{Me}$**−**Ni** can be described as an almost unmodified picture of the Gouterman "four-orbital" model based on the D_{4h} symmetric porphyrin and metalloporphyrin entities,[32] with proper modifications taking into account the lower symmetry of the here investigated asymmetrically *meso*-substituted porphyrins and the extended conjugation over the triple bond of the ethynyl moiety.[28b] Further details including frontier molecular orbital (FMO) description, isodensity surface plots, and FMO energy level can be found in section 2.2 of the Supporting Information.

Starting from the optimized geometries of **T$_{Me}$** and **T$_{Me}$**−**Ni**, we performed a computational investigation of the electronic

a)

T_{Me}

$T_{Me}-Ni$

b)

$[T_{Me}(CoCl_2)]$
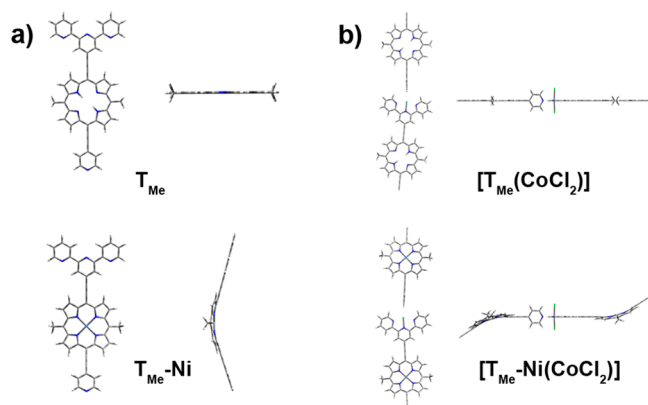
$[T_{Me}-Ni(CoCl_2)]$

Figure 1. Top and side views of the (a) DFT-optimized ground-state geometry minima with C_s symmetry found for compounds T_{Me} and $T_{Me}-Ni$ in the gas phase and (b) DFT-modeled 1D array structures of $[T_{Me}(CoCl_2)]$ and $[T_{Me}-Ni(CoCl_2)]$.

properties on the open-shell cobalt(II)-containing derivatives with a formal d^7 electronic configuration on the Co metal center, namely, $[T_{Me}(CoCl_2)]$ and $[T_{Me}-Ni(CoCl_2)]$, at their electronic ground-state geometry at the DFT level of theory. For these compounds, we needed to adopt a simplified version of the ideal infinite array because of computational accessibility. The modeled structures are displayed in Figure 1b, and the corresponding energies are listed in Table S2 in the Supporting Information. For the computed $[T_{Me}(CoCl_2)]$ and $[T_{Me}-Ni(CoCl_2)]$ derivatives, the unrestricted formalism of the B3LYP functional (UB3LYP) was employed at the same level of theory used for the T_{Me} and $T_{Me}-Ni$ derivatives. As far as the cobalt(II) core moiety is concerned, we found that the quartet electronic configuration resulted in the lowest energy minimum,[33] in which the tridentate terpyridyl moiety coordinated to the d^7 Co(II) atom adopts a clearly distorted conformation as a consequence of the Jahn–Teller effect, with Co–N_{tpy} bond lengths of 2.256 and 2.186 Å, where N_{tpy} is the coordinating nitrogen of the two side pyridines of the tpy ligand, and a Cl–Co–Cl bond angle of 175.9°.

Analysis of the electronic structure of compounds $[T_{Me}(CoCl_2)]$ and $[T_{Me}-Ni(CoCl_2)]$ appears more intricate at first glance also as a consequence of the overall open-shell nature of the systems. Nevertheless, it is possible to observe that the π and π^* FMO spin–orbitals corresponding to the porphyrin moieties are paired in their α and β spins in both nature and energy; thus, for the sake of clarity, we will hereafter refer to the α spin–orbital component only. As far as $[T_{Me}(CoCl_2)]$ is concerned, the overall FMO diagram agrees well with the Gouterman four-orbital model for the monomeric porphyrin counterpart, taking into account the dimeric nature of the system,[28b,c] and the imposed asymmetry coming from the model fragment used for studying the 1D array. Overall, the computed electronic structure corresponds to noninteracting porphyrin system in which the absence of electronic communication at the electronic ground state between neighbor porphyrin rings is ascribed to the interruption of the conjugation due to the presence of the $^4[CoCl_2(terpy)-(py)]$ moiety in between. Nonetheless, a singly occupied FMO with d(Co)p(Cl) character, namely, the highest occupied molecular orbital (HOMO) − 2 (α), is found to lie at −5.240 eV, namely, an energetic level that is between those of the two sets of π FMOs within the four-orbital description.

As discussed above, the binding of the Ni(II) cation by the central core of the porphyrin in $[T_{Me}-Ni(CoCl_2)]$ is expected to sizably influence the geometrical and electronic properties of the molecular system with respect to the metal-free counterpart $[T_{Me}(CoCl_2)]$. In particular, the nickel(II) porphyrin core adopts a ruffled geometry, which is expected to slightly flatten with respect to that computed in the gas phase, as a result of the interaction with the solid HOPG surface, although a full planarization of the geometry might be ruled out. As far as the orbital analysis is concerned, a stabilization of the filled α spin FMOs is observed in the MO energy diagram of $[T_{Me}-Ni(CoCl_2)]$, the larger energy difference being for the highest singly occupied molecular orbital (HSOMO) (see Table S2 and Figures S11 and S12 in the Supporting Information). Similarly to $[T_{Me}(CoCl_2)]_n$, also for derivative $[T_{Me}-Ni(CoCl_2)]$ the four-orbital model can still be observed where the highest singly occupied FMO located on the $^4[CoCl_2(terpy)(py)]$ moiety with d(Co)p(Cl) character corresponds now to the HOMO − 1 (α). Finally, it is worth noticing that the HSOMO to HOMO − 6 levels lie in a narrow overall energetic window of 0.65 eV.

2.3. Photophysical and TD-DFT Characterization. Figure 2 displays the UV−vis absorption spectra of **T** and
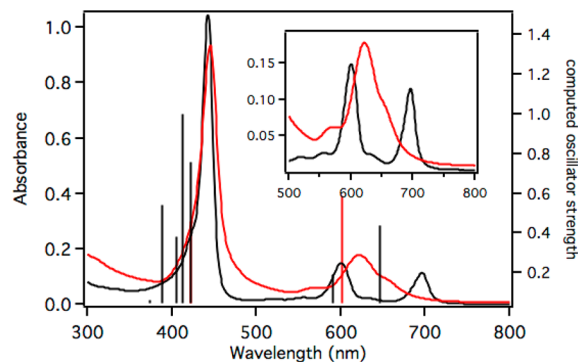
Figure 2. Room-temperature absorption spectra of **T** (black) and **T−Ni** (red) in CHCl$_3$ solution at a concentration of 0.1 mM (solid traces) and comparison with the computed vertical excitation by means of TD-DFT (vertical bars). Inset: magnified view of the Q-band region.

T−Ni recorded in CHCl$_3$. For both tectons **T** and **T−Ni**, their electronic optical properties were also jointly investigated by time-dependent DFT (TD-DFT) at the same level of theory used for the ground-state optimization and electronic property analysis (see the above text and the Experimental Section for more details).

Both compounds **T** and **T−Ni** exhibit the characteristic porphyrin absorption spectra consisting of the following: (i) A strong Soret band in the higher energy region ($\lambda_{max} = 445$ nm) which can be ascribed to the convolution of four strongly allowed excitation processes calculated at 388 nm ($f = 0.54$), 405 nm ($f = 0.38$), and 413 nm ($f = 1.0$) corresponding to the HOMO − 4 → LUMO (lowest occupied molecular orbital) and an admixture of HOMO → LUMO + 2 and HOMO/HOMO − 1 → LUMO + 2/LUMO + 1/LUMO one-electron excitation processes, respectively, for compound T_{Me}. On the other hand, a strong excitation process is calculated at 422 nm ($f = 0.76$) attributed to the HOMO/HOMO − 1 → LUMO + 1/LUMO electronic transition. (ii) A weaker Q-band in the lower energy region between 500 and 750 nm. This band is computed at 646 and 601 nm for T_{Me} and $T_{Me}-Ni$,
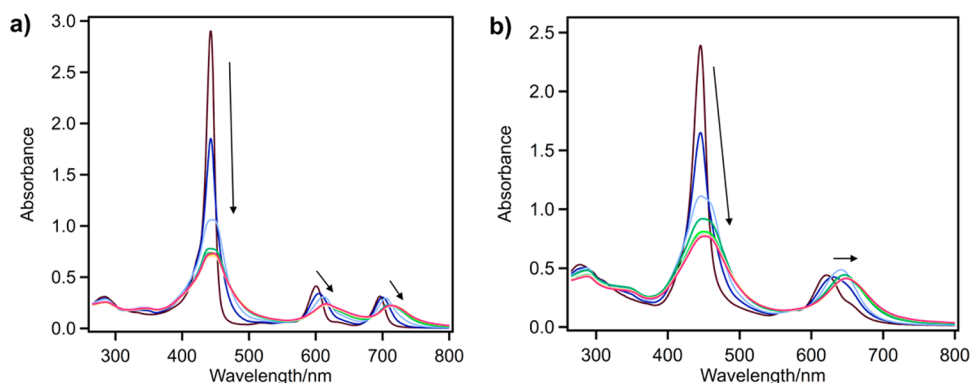
Figure 3. Spectrophotometric titration of 0.1 mM (a) **T** and (b) **T−Ni** using for each titration step 1 μL of CoCl$_2$ solution (*c* = 8.2 mM) upon addition of 1 μL aliquots in DMF.

respectively, with a much weaker oscillator strength (*f* = 0.44 and 0.59, respectively) and corresponds for both compounds to the HOMO → LUMO transition, as typical of porphyrin derivatives.[28a,b] Such a hypsochromic shift of 1160 cm^{-1} observed in the computed transitions going form **T$_{Me}$** to **T$_{Me}$−Ni** is in good agreement with the experimental finding (1098 cm^{-1}). Interestingly, both **T** and **T−Ni** show a very slight broadening and red-shifted Q-bands, while the Soret band is considerably less intense than that of a standard *meso*-tetraphenylporphyrin.[34] These spectral perturbations can be due to the extended conjugation of these molecules. Moreover, other bands are seen below 400 nm, which can be attributed to π−π* transitions localized on the terpyridine ligands (280 nm).[8b]

To gain a deeper understanding of the formation of both complexes, we performed spectrophotometric titration of **T** and **T−Ni** by CoCl$_2$ (Figure 3). Upon titration using a 1 μL increment of CoCl$_2$ solution, **T** and **T−Ni** show a markedly reduced, broadened, and slightly red-shifted Soret peak, a reduced height of the Q-band, and new bands, very broad and red-shifted at around 615 and 715 nm for **T** and 660 nm for **T−Ni**.

This effect observed for both ligands **T** and **T−Ni** indicates that the spectral changes result from the binding of CoCl$_2$ by the peripheral terpyridyl/pyridyl units and not by the inner core of the porphyrin. Because of the presence of ethynyl bridges in **T** and **T−Ni**, the conjugation of the molecules can only be interrupted by the complexation of Co(II) ions. Dramatic spectral changes observed upon addition of CoCl$_2$ correspond to charge transfer interactions with *para*-substituents,[19b] and represent a characteristic feature of hyperporphyrin spectra. Noteworthy, the absence of an isosbestic point can be ascribed to the formation of insoluble particles, which appear in the solution after complexation, and can be attributed to the [**T**(CoCl$_2$)]$_x$ and/or [**T−Ni**(CoCl$_2$)]$_x$ polymeric species.

2.4. Scanning Tunneling Microscopy. Tecton **T** and metallatecton **T−Ni** are both acentric units offering two peripheral coordinating poles based on a monodentate pyridyl site and a tridentate terpyridyl moiety. Their interconnection leading to extended periodic 1D architectures may be achieved using a 4-connecting metallic node with square planar geometry. We have exploited CoCl$_2$, i.e., a neutral entity that forms octahedral complexes for which the two chloride anions occupy the apical positions. Such a Co(II) center may be used as a 4-connecting unit to bridge consecutive tectons **T** or **T−**

Ni. Owing to the acentric nature of the tecton **T** and metallatecton **T−Ni**, their interconnection by a 4-connecting metallic node such as CoCl$_2$ must lead to an inherently directional 1D homometallic or heterobimetallic coordination network, respectively (Figure 4).
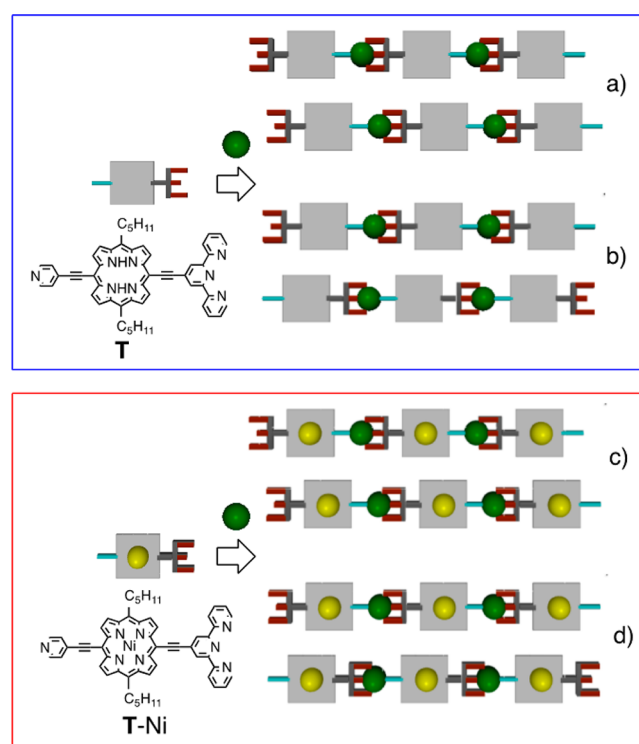
Figure 4. Schematic representation of the homometallic and heterobimetallic Ni(II) (yellow spheres) and 1D directional Co(II) (green spheres) coordination networks resulting from the bridging of consecutive tectons **T** or metallatectons **T−Ni** by CoCl$_2$ behaving as a 4-connecting node and the *syn* (a, c) and *anti* (b, d) parallel packing of consecutive networks.

The generation of 1D coordination networks was achieved at the solid/liquid interface on an HOPG surface. The self-assembly process was monitored by STM. The organization of the free tecton **T** was first studied by casting a 4 μL drop of a 0.1 mM solution of **T** in 1-phenyloctane onto the HOPG surface. Figure 5a displays the STM image of the monolayer formed, indicating the formation of a 2D ordered structure.
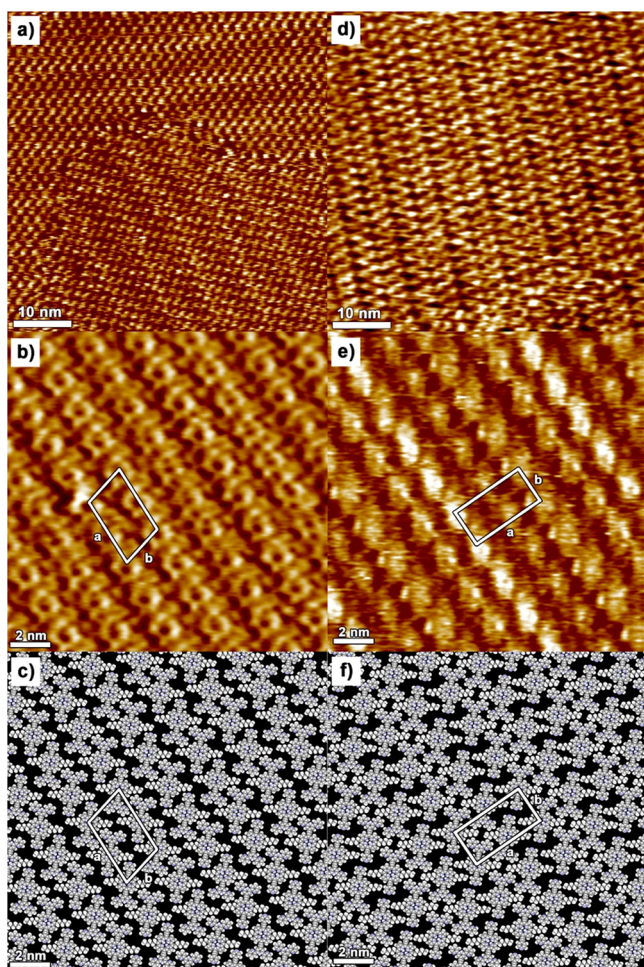
Figure 5. STM images of the **T** networks formed at the 1-phenyloctane solution/HOPG interface: (a) survey height STM image; (b) current STM image, zoom-in; (c) representative model of the **T** 2D pattern. STM images of **T−Ni** networks: (d) survey height STM image; (e) height STM image, zoom-in; (f) representative model of the **T−Ni** 2D pattern. Tunneling parameters: (a) I_t (average tunneling current) = 25 pA, V_t (tip bias) = −750 mV; (b) I_t = 25 pA, V_t = −800 mV; (d) I_t = 25 pA, V_t = −700 mV; (e) I_t = 25 pA, V_t = −650 mV.

On a smaller scale, the pattern reveals a lamellar motif extended in 2D (Figure 5b). For all crystalline 2D patterns the unit cell parameters, i.e., the length of the vectors a and b, the angle between the vectors (α), the unit cell area (A), the number of molecules in the unit cell (N_{mol}), and the area occupied by a single molecule in the unit cell (A_{mol}, with $A_{mol} = A/N_{mol}$) are reported in Table 1.

It is important to notice that when the HOPG substrate is negatively biased, the electrons will flow from the sample to the Pt/Ir tip, assisted by the orbital aligned between the electrodes, which in this particular case is expected to arise from the

tunneling of the highest occupied molecular orbitals of tecton **T** on the basis of the applied V_t. As can be seen in Figure 5b, within a 2D ordered pattern, each lamella is a linear array of circular features with empty cavities, which can be assigned to the porphyrin core of **T**. As discussed in the previous section, HOMOs of tectons **T** are delocalized on the porphyrin ring and the ethynyl moieties, with a relatively small contribution of the pyridyl rings linked to the porphyrin, and both possess a″ symmetry; therefore, the specific positions of both pyridyl and terpyridyl units cannot be unambiguously singled out from the STM image (see Figure S14 in the Supporting Information). Nevertheless, the analysis of the unit cell parameters, and in particular its area A, along with the contrast in the images suggests that the molecules exhibit an *anti*-parallel orientation both within each lamella and also in adjacent lamellae, in a packing motif characterized by a minimization of the area occupied by the single molecule **T**; i.e., the molecular density on the HOPG is maximized. Such a self-assembled motif can be expected to be thermodynamically favored since it can be stabilized by the minimization of dipolar interactions.[35] The proposed molecular packing model is shown in Figure 5c.

The self-assembly behavior of the metallatecton **T−Ni** was also investigated by STM. It revealed the formation of a 2D crystalline structure (Figure 5d) comprising a dimerlike lamellar motif (Figure 5e). The unit cell parameters extracted from the **T−Ni** ordered pattern (Table 1) are markedly different from those obtained for **T**. Noteworthy, the small ionic radius of 0.69 Å for Ni(II) present in the core of the **T−Ni** porphyrin tends to pull the pyrrole nitrogen atoms inward and contract the core,[36] resulting in small deformations of the porphyrin core with respect to the fully planar conformation of **T** (see the discussion in section 2.2). Therefore, the porphyrin core of **T−Ni** appears as bright protrusions (as observed in Figure 5e), rather than hollow structures as in the case of **T**. Similar observations have been reported for STM characterization of metal-free vs iron porphyrins under ultrahigh vacuum (UHV).[37] Moreover, the presence of nickel in the porphyrin core leads to a different **T−Ni** self-assembly pattern when compared to the one observed for the free **T**. The **T−Ni** ribbons, composed of two rows of tectons, display a smaller intraspacing than the distance between the ribbons (see Figure S16 from ex situ in the Supporting Information), which can suggest the formation of crystalline monolayers in which the tectons belonging to the same ribbon exhibit the same orientation whereas they display an opposite orientation in adjacent ribbons, as shown in the proposed packing motif in Figures 5f and S14 in the Supporting Information. The difference in the STM imaging contrast between adjacent **T−Ni** metallatectons is the result of the Moiré effect, i.e., the electronic mismatch/interference of the supramolecular lattice and the underlying HOPG surface.

The investigation was extended to the in situ and ex situ formation of 1D directional coordination networks using $CoCl_2$ as a 4-connecting node and their packing on the HOPG

Table 1. Unit Cell Parameters of the Structures T, T−Ni, $[T(CoCl_2)]_n$, and $[T−Ni(CoCl_2)]_n$

structure	a (nm)	b (nm)	α (deg)	A (nm²)	N_{mol}	A_{mol} (nm²)
T	3.6 ± 0.1	2.3 ± 0.1	75 ± 2	3.9 ± 0.2	1	3.9 ± 0.2
T−Ni	3.9 ± 0.1	2.0 ± 0.1	90 ± 2	7.8 ± 0.4	2	3.9 ± 0.2
$[T(CoCl_2)]_n$	2.9 ± 0.1	2.6 ± 0.1	90 ± 2	7.7 ± 0.3	2	3.9 ± 0.2
$[T−Ni(CoCl_2)]_n$	4.9 ± 0.1	2.5 ± 0.1	68 ± 2	11.3 ± 0.5	3	3.8 ± 0.3

surface. As a first attempt, in situ experiments have been carried out by the addition of 1 equiv of $CoCl_2 \cdot 2H_2O$ on the top of a pre-existing monolayer of **T**. To this end, a 4 μL drop of a 0.1 mM solution (isopropanol/1-phenyloctane, 1:99, v/v) was deposited on top of a monolayer of **T** previously formed by applying a 4 μL drop of a 0.1 mM solution of **T** in 1-phenyloctane on the HOPG surface. The recorded STM image of the monolayer is shown in Figure 6a.
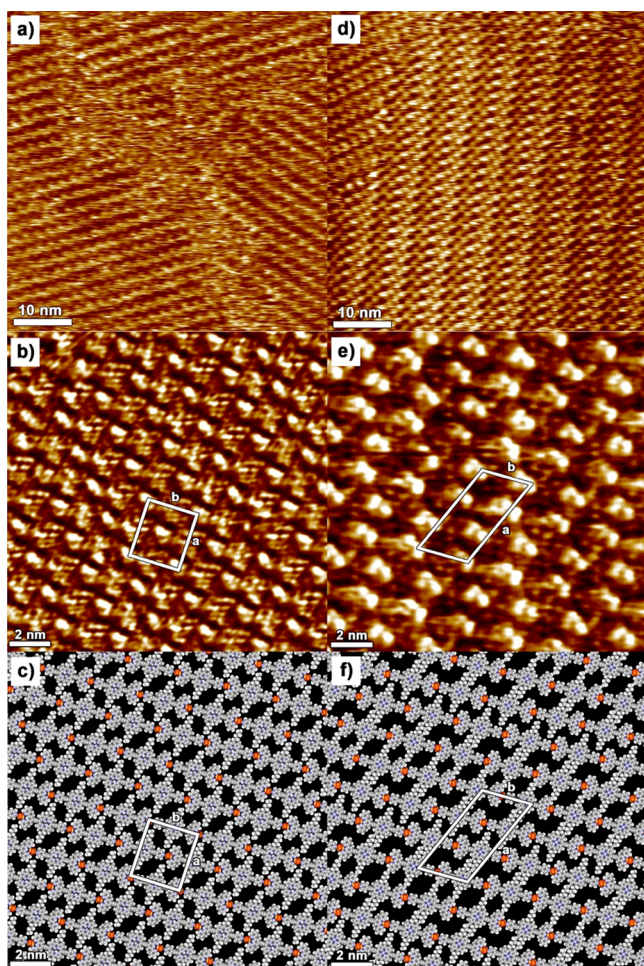
Figure 6. STM images of the 2D network of $[\mathbf{T}(CoCl_2)]_n$ formed at the 1-phenyloctane solution/HOPG interface: (a) survey height STM image; (b) current STM image, zoom-in; (c) representative model of the $[\mathbf{T}(CoCl_2)]_n$ network. STM images of the bimetallic network $[\mathbf{T}-Ni(CoCl_2)]_n$: (d) survey height STM image; (e) height STM image, zoom-in; (f) representative model of the $[\mathbf{T}-Ni(CoCl_2)]_n$ network. Tunneling parameters: (a) I_t (average tunneling current) = 25 pA, V_t (tip bias) = −700 mV; (b) I_t = 25 pA, V_t = −600 mV; (d) I_t = 25 pA, V_t = −700 mV; (e) I_t = 30 pA, V_t = −550 mV.

According to our previous observations,[20b,35] the combination of the neutral tectons **T** or **T**−Ni bearing pyridyl and terpyridyl binding poles with $CoCl_2$ should lead to the formation of 1D directional coordination networks on the graphite surface. The STM height image in Figure 6a exhibits a crystalline monolayer consisting of ordered 1D coordination networks laterally interacting via van der Waals forces (for unit cell parameters, see Table 1). The STM image in Figure 6b exhibits bright spots regularly spaced, which can be ascribed to both the pyridyl−Co(II)−terpyridyl coordination nodes and the porphyrin rings located on the surface. Such a bright

contrast is further supported by the energetic proximity of the filled singly occupied FMOs located on the $[CoCl_2(terpy)(py)]$ with d(Co)p(Cl) character and the π orbitals of the porphyrin ring as displayed in Figures S11 and S12 (see the Supporting Information). For comparison, in Figure S10 (see the Supporting Information) is shown an overlay of the four and six highest α spin−orbital FMOs, which lie within an energetic proximity as close as 0.6 and 0.45 eV for the DFT-investigated $[\mathbf{T}(CoCl_2)]_n$ and $[\mathbf{T}-Ni(CoCl_2)]_n$ derivatives, respectively (see section 2.2). The distance of 2.44 ± 0.1 nm between consecutive Co(II) metallic nodes, i.e., the length of vector b of the unit cell, matches the contour length of a single tecton **T**. This confirms that 1D $[\mathbf{T}(CoCl_2)]_n$ neutral coordination networks are formed upon bridging of consecutive neutral tectons **T** by neutral $CoCl_2$ salt. The surroundings of the cobalt(II) cation are composed of four N atoms of a terpyridyl unit and a pyridyl unit belonging to two consecutive tectons **T**. Noteworthy, because of the limited spatial resolution in the STM images, unambiguous determination of the directionality in consecutive $[\mathbf{T}(CoCl_2)]_n$ rows is not possible. Nevertheless, our previous studies[20b,35] show that the 1D coordination networks are typically formed in the *anti*-parallel fashion (Figure 4b), leading thus to an apolar thermodynamically favored pattern (Figure 6b). Both possible packing motifs, i.e., *anti*-parallel and *syn*-parallel, are shown in Figure S21 (Supporting Information).

The formation of a 1D directional heterobimetallic (Ni, Co) coordination network on an HOPG surface was also investigated upon combining the metallatecton **T**−Ni with $CoCl_2$. As in the case of in situ formation of the homometallic $[\mathbf{T}(CoCl_2)]_n$ network, an equimolar amount of $CoCl_2 \cdot 2H_2O$ in solution was deposited onto the **T**−Ni monolayer. The STM study revealed an unprecedented formation of an ordered pattern composed of heterobinuclear directional coordination networks on the surface (Figure 6e). The pattern consists of the 2D organization of the self-assembled 1D coordination networks. The distance of 2.5 ± 0.1 nm between two aligned motifs (within the same array), i.e., the length of vector b, matches the length of a single **T**−Ni tecton. This observation confirms the formation of the coordination networks $[\mathbf{T}-Ni(CoCl_2)]_n$ on the graphite surface. In marked contrast with the case of the $[\mathbf{T}(CoCl_2)]_n$ homometallic coordination network for which consecutive 1D architectures are packed in an *anti*-parallel fashion (Figure 6b), for the heterobimetallic 1D network $[\mathbf{T}-Ni(CoCl_2)]_n$, the packing, although again centric, is different (Figure 6e). Indeed, within the 2D ordered organization on the HOPG surface, two adjacent 1D networks are most likely arranged in a *syn*-parallel manner (Figure 4c), and the next pair is rotated by 180°, leading thus to an overall AABB centric packing mode generating a nonpolar arrangement; however an *anti*-parallel arrangement can also be considered (see Figure S22 in the Supporting Information). Furthermore, as discussed previously (see section 2.2), owing to the nonplanarity of **T**−Ni tectons, the bright protrusions observed can be ascribed to nickel-coordinated porphyrin and not to the pyridyl−Co(II)−terpyridyl coordination nodes as in the case of $[\mathbf{T}(CoCl_2)]_n$. Importantly, even though the unit cell parameters of $[\mathbf{T}(CoCl_2)]_n$ and $[\mathbf{T}-Ni(CoCl_2)]_n$ are different, the areas of single $\mathbf{T}(CoCl_2)$ and $\mathbf{T}-Ni(CoCl_2)$ repetitive units within the 1D coordination networks are equal.

Interestingly, the unit cell parameters of the self-assembled structures of both coordination polymers prepared ex situ

perfectly match those obtained from in situ complexation (see the Supporting Information).

2.5. Electrochemical Measurements. We have also performed electrochemical analyses of all compounds investigated both in solution and when physisorbed on an HOPG substrate (see section 4 of the Supporting Information for details). Initially, we carried out the electrochemical experiments in CHCl$_3$. **T** displays three irreversible oxidation processes peaking at 1.05, 1.29, and 1.65 V and two irreversible reduction processes peaking at −0.92 and −1.26 V. The insertion of the Ni(II) ion within the porphyrin tetraaza macrocyclic moiety (**T−Ni**) leads to the formation of a new quasi-reversible oxidation process with $E_{1/2}$ = 0.57 V which can be assigned to the oxidation of the metal center ion to give Ni(III). Unfortunately, $[\mathbf{T}(\text{CoCl}_2)]_n$ and $[\mathbf{T−Ni}(\text{CoCl}_2)]_n$ could not be measured in solution due to their very poor solubility in organic solvents. To overcome this problem, we prepared a homemade working electrode by connecting commercial HOPG to the copper wire (see the Supporting Information for details). This allowed evaluation of the electronic effect of the tecton **T** and metallatecton **T−Ni** as well as of their coordination network formed on the HOPG surface upon addition of CoCl$_2$ as the connecting metallic center. Both **T** and **T−Ni** on HOPG showed different patterns when compared to measurements performed in solution, indicating that the surface plays an important role in the final electronic properties of the components. In particular, **T** is characterized by two sharp irreversible oxidation peaks at 1.32 and 1.20 V, while in **T−Ni**, such peaks are anodically shifted to 1.51 and 1.28 V, respectively, in agreement with the trend observed in solution. Interestingly, the presence of Co(II) leads to a shift of the oxidation processes to lower potential for both $[\mathbf{T}(\text{CoCl}_2)]_n$ and $[\mathbf{T−Ni}(\text{CoCl}_2)]_n$. However, while for $[\mathbf{T}(\text{CoCl}_2)]_n$ two oxidation processes at 1.28 and 1.07 V can still be distinguished, for $[\mathbf{T−Ni}(\text{CoCl}_2)]_n$ only a broad peak is observed at 1.20 V.

3. CONCLUSION

In conclusion, by combining the molecular tectonics approach at the solid/liquid interface with in situ STM nanoscale-resolved imaging, 1D directional coordination networks resulting from interconnection of acentric coordinating tectons **T** and **T−Ni** based on a porphyrin backbone bearing two differentiated coordinating poles (pyridyl and terpyridyl units) with CoCl$_2$ could be generated on the graphite surface. Interestingly, whereas the combination of the metal-free tecton **T** leads to the formation of a 1D directional homometallic coordination network, the metallatecton **T−Ni**, obtained upon metalation of the porphyrin core Ni(II) cation, affords an unprecedented example of a 1D heterobimetallic directional architecture on the HOPG surface. In both cases, the packing of directional 1D networks leads to a centric and ordered organization on the surface.

The ability to incorporate two distinct metallic centers possessing different electronic and optical properties at predefined positions paves the way toward the bottom-up construction of robust multicomponent and , thus, multifunctional molecular nanostructures and nanodevices in which the metal centers can be addressed individually to modulate the fundamental properties of interest, e.g., in electrochemistry, storage, and/or spintronics.

4. EXPERIMENTAL SECTION

All reagents were purchased from commercial sources and used without further purification, except for pyrrole, NBS, AsPh$_3$, and CuI. The support used for chromatography was Geduran silica gel Si60 (40−63 μm) from Merck and aluminum oxide 90 standardized from Merck. ^{1}H NMR and ^{13}C NMR spectra were recorded at room temperature on Bruker NMR spectrometers. UV−vis absorption spectra performed in CH$_2$Cl$_2$ were collected at room temperature on a UVIKON XL spectrometer from BIO-TEK instruments. UV−vis absorption spectra performed in CHCl$_3$ were recorded on a Jasco V-670 spectrophotometer. IR spectra were recorded using a PerkinElmer spectrometer (Spectrum Two) equipped with attenuated total reflectance (ATR) diamond. Mass spectra (ESI-MS) were recorded on a micro-TOF LC spectrometer (Bruker Daltonics, Bremen, Germany).

Dipyrromethane,[38] 5,15-dipentylporphyrin **1**,[24] ethynylpyridine **3**,[25] and ethynylterpyridine **5**[11f] were synthesized according to the described procedure (see the Supporting Information).

4.1. Scanning Tunneling Microscopy. STM measurements were performed using a Veeco scanning tunneling microscope (Multimode Nanoscope III, Veeco) at the interface between an HOPG substrate and a supernatant solution, thereby mapping a maximum area of 1 × 1 μm. The solution of molecules was applied to the basal plane of the surface. For STM measurements, the substrates were glued to a magnetic disk and an electric contact was made with silver paint (Aldrich Chemicals). The STM tips were mechanically cut from a Pt/Ir wire (90:10, diameter 0.25 mm). The raw STM data were processed through the application of background flattening, and the drift was corrected using the underlying graphite lattice as a reference. The lattice was visualized by lowering the bias voltage to 20 mV and raising the current to 65 pA. **T** and **T−Ni** were dissolved in CHCl$_3$ and diluted with 1-phenyloctane to give 0.1 mM solutions. STM imaging was carried out in constant-height mode without turning off the feedback loop to avoid tip crashes. CoCl$_2$·2H$_2$O was solubilized in isopropanol (*i*-PrOH) at a concentration (*c*) of 10 mM and further diluted with 1-phenyloctane to give a concentration of 0.1 mM. Monolayer pattern formation was achieved by applying 4 μL of a solution onto a freshly cleaved HOPG surface. The STM images were recorded at room temperature once a negligible thermal drift was achieved. All of the molecular models were minimized with MMFF and processed with QuteMol visualization software (http://qutemol.sourceforge.net).

4.2. Computational Details. Ground-state (S$_0$) geometries were optimized without symmetry constraints by means of DFT employing either the restricted or the unrestricted formalism of the exchange-correlation hybrid functional (U)B3LYP.[39] The standard valence double-ζ polarized basis set 6-31G(d,p)[40] was used for C, H, N, and Cl. For Co and Ni, the LANL2DZ effective core potential (ECP) was employed along with the corresponding basis set. Optimization of the model cobalt complex [CoCl$_2$(terpy)py], where terpy is 2,2′:6′,2″-terpyridine and py is pyridine, was performed at its ground state at both doublet and quartet electronic configurations to obtain the corresponding minimum-energy configuration, while for derivatives [$\mathbf{T_{Me}}$(CoCl$_2$)] and [$\mathbf{T_{Me}}$−Ni(CoCl$_2$)] single-point calculations were performed starting from the corresponding DFT-optimized geometries of both the [CoCl$_2$(terpy)py] complex and porphyrinic moieties. The geometrical parameters of all the computed molecules are reported as Cartesian coordinates embedded into an XYZ file in the Supporting Information; thus, that they can be easily manipulated with molecular visualization program packages (e.g., Mercury). To simulate the absorption electronic spectrum, for compounds $\mathbf{T_{Me}}$ and $\mathbf{T_{Me}}$−Ni the lowest 10 singlet-manifold (S$_0$ → S$_n$, n = 1−10) excitations were computed in vacuum on the optimized geometry with C_s symmetry at the S$_0$ state by means of TD-DFT at the same level of accuracy as the ground state. The computed vertical transitions are described in terms of one-electron excitations involving MOs of the corresponding S$_0$ geometry. All the calculations were performed with the Gaussian09 program package.[41]

Article

■ ASSOCIATED CONTENT

S Supporting Information

Description of the synthesis and characterization of **T** and **T**−Ni tectons, detailed computational (DFT) analysis, cyclic voltammetry measurements, and coordinates of all computed structures (XYZ file). The Supporting Information is available free of charge on the ACS Publications website at DOI: 10.1021/jacs.5b02283.

■ AUTHOR INFORMATION

Corresponding Authors
*ciesielski@unistra.fr
*bulach@unistra.fr
*hosseini@unistra.fr
*samori@unistra.fr

Notes
The authors declare no competing financial interest.

■ ACKNOWLEDGMENTS

■ REFERENCES

(1) (a) Simard, M.; Su, D.; Wuest, J. D. J. Am. Chem. Soc. 1991, 113, 4696. (b) Mann, S. Nature 1993, 365, 499. (c) Desiraju, G. R. Acc. Chem. Res. 2002, 35, 565. (d) Hosseini, M. W. CrystEngComm 2004, 6, 318. (e) Hosseini, M. W. Acc. Chem. Res. 2005, 38, 313. (f) Hosseini, M. W. Chem. Commun. 2005, 5825.

(2) (a) Batten, S. R.; Robson, R. Angew. Chem., Int. Ed. 1998, 37, 1460. (b) Swiegers, G. F.; Malefetse, T. J. Chem. Rev. 2000, 100, 3483. (c) Eddaoudi, M.; Moler, D. B.; Li, H.; Chen, B.; Reineke, T. M.; O'Keeffe, M.; Yaghi, O. M. Acc. Chem. Res. 2001, 34, 319. (d) Moulton, B.; Zaworotko, M. J. Chem. Rev. 2001, 101, 1629. (e) Janiak, C. Dalton Trans. 2003, 2781. (f) Kitagawa, S.; Kitaura, R.; Noro, S.-i. Angew. Chem., Int. Ed. 2004, 43, 2334. (g) Férey, G.; Mellot-Draznieks, C.; Serre, C.; Millange, F. Acc. Chem. Res. 2005, 38, 217. (h) Yu, L.; Lindsey, J. S. J. Org. Chem. 2001, 66, 7402.

(3) Abrahams, B. F.; Hoskins, B. F.; Robson, R. J. Am. Chem. Soc. 1991, 113, 3606.

(4) (a) Khlobystov, A. N.; Blake, A. J.; Champness, N. R.; Lemenovskii, D. A.; Majouga, A. G.; Zyk, N. V.; Schröder, M. Coord. Chem. Rev. 2001, 222, 155. (b) Leong, W. L.; Vittal, J. J. Chem. Rev. 2010, 111, 688. (c) Moulton, B.; Zaworotko, M. J. Chem. Rev. 2001, 101, 1629. (d) Ockwig, N. W.; Delgado-Friedrichs, O.; O'Keeffe, M.; Yaghi, O. M. Acc. Chem. Res. 2005, 38, 176. (e) Zhou, H.-C.; Long, J. R.; Yaghi, O. M. Chem. Rev. 2012, 112, 673.

(5) (a) Barron, P. M.; Son, H.-T.; Hu, C.; Choe, W. Cryst. Growth Des. 2009, 9, 1960. (b) Baudron, S. A. CrystEngComm 2010, 12, 2288. (c) Béziau, A.; Baudron, S. A.; Fluck, A.; Hosseini, M. W. Inorg. Chem. 2013, 52, 14439. (d) Béziau, A.; Baudron, S. A.; Pogozhev, D.; Fluck, A.; Hosseini, M. W. Chem. Commun. 2012, 48, 10313. (e) Béziau, A.; Baudron, S. A.; Rasoloarison, D.; Hosseini, M. W. CrystEngComm 2014, 16, 4973. (f) Burrows, A. D. CrystEngComm 2011, 13, 3623. (g) Choi, E.-Y.; Barron, P. M.; Novotny, R. W.; Son, H.-T.; Hu, C.; Choe, W. Inorg. Chem. 2008, 48, 426. (h) Das, M. C.; Xiang, S.; Zhang, Z.; Chen, B. Angew. Chem., Int. Ed. 2011, 50, 10510. (i) Deiters, E.; Bulach, V.; Hosseini, M. W. Dalton Trans. 2007, 4126. (j) Farha, O. K.;

Shultz, A. M.; Sarjeant, A. A.; Nguyen, S. T.; Hupp, J. T. J. Am. Chem. Soc. 2011, 133, 5652. (k) Kumar, G.; Gupta, R. Chem. Soc. Rev. 2013, 42, 9403. (l) Suslick, K. S.; Bhyrappa, P.; Chou, J.-H.; Kosal, M. E.; Nakagaki, S.; Smithenry, D. W.; Wilson, S. R. Acc. Chem. Res. 2005, 38, 283.

(6) (a) Jouaiti, A.; Hosseini, M. W.; De Cian, A. Chem. Commun. 2000, 1863. (b) Jouaiti, A.; Hosseini, M. W.; Kyritsakas, N. Chem. Commun. 2002, 1898. (c) Jouaiti, A.; Jullien, V.; Hosseini, M. W.; Planeix, J.-M.; De Cian, A. Chem. Commun. 2001, 1114.

(7) Furukawa, S.; De Feyter, S. In Templates in Chemistry III; Broekmann, P., Dötz, K.-H., Schalley, C., Eds.; Springer: Berlin, Heidelberg, 2009; Vol. 287, p 87.

(8) (a) Cargill Thompson, A. M. W. Coord. Chem. Rev. 1997, 160, 1. (b) Schubert, U. S.; Hofmeier, H.; Newkome, G. R. Modern Terpyridine Chemistry; John Wiley & Sons: Weinheim, Germany, 2006.

(9) Liang, W.; Shores, M. P.; Bockrath, M.; Long, J. R.; Park, H. Nature 2002, 417, 725.

(10) Barboiu, M.; Lehn, J.-M. Proc. Natl. Acad. Sci. U.S.A. 2002, 99, 5201.

(11) (a) Rosei, F.; Schunack, M.; Jiang, P.; Gourdon, A.; Lægsgaard, E.; Stensgaard, I.; Joachim, C.; Besenbacher, F. Science 2002, 296, 328. (b) De Feyter, S.; De Schryver, F. C. Chem. Soc. Rev. 2003, 32, 139. (c) Bonifazi, D.; Spillmann, H.; Kiebele, A.; de Wild, M.; Seiler, P.; Cheng, F.; Güntherodt, H.-J.; Jung, T. A.; Diederich, F. Angew. Chem., Int. Ed. 2004, 43, 4759. (d) Wan, L. J. Acc. Chem. Res. 2006, 39, 334. (e) Bonifazi, D.; Kiebele, A.; Stöhr, M.; Cheng, F.; Jung, T.; Diederich, F.; Spillmann, H. Adv. Funct. Mater. 2007, 17, 1051. (f) Sasaki, T.; Guerrero, J. M.; Tour, J. M. Tetrahedron 2008, 64, 8522. (g) MacLeod, J. M.; Ivasenko, O.; Fu, C.; Taerum, T.; Rosei, F.; Perepichka, D. F. J. Am. Chem. Soc. 2009, 131, 16844.

(12) Samorì, P. Scanning Probe Microscopies beyond Imaging: Manipulation of Molecules and Nanostructures; John Wiley & Sons: Weinheim, Germany, 2006.

(13) (a) Gesquière, A.; De Feyter, S.; Schoonbeek, F.; van Esch, J.; Kellogg, R. M.; Feringa, B. L. Nano Lett. 2001, 1, 201. (b) Klappenberger, F.; Kühne, D.; Krenner, W.; Silanes, I.; Arnau, A.; García de Abajo, F. J.; Klyatskaya, S.; Ruben, M.; Barth, J. V. Nano Lett. 2009, 9, 3509. (c) Auwärter, W.; Seufert, K.; Klappenberger, F.; Reichert, J.; Weber-Bargioni, A.; Verdini, A.; Cvetko, D.; Dell'Angela, M.; Floreano, L.; Cossaro, A.; Bavdek, G.; Morgante, A.; Seitsonen, A. P.; Barth, J. V. Phys. Rev. B 2010, 81, 245403. (d) El Garah, M.; Palmino, F.; Chérioux, F.; Melinte, S.; Hackens, B.; Rodrigues, M. S.; Bogdan, D.; Duverger, E. Phys. Rev. B 2012, 85, 035425. (e) Seufert, K.; Auwärter, W.; García de Abajo, F. J.; Ecija, D.; Vijayaraghavan, S.; Joshi, S.; Barth, J. V. Nano Lett. 2013, 13, 6130. (f) Jackson, A. M.; Myerson, J. W.; Stellacci, F. Nat. Mater. 2004, 3, 330. (g) Riss, A.; Wickenburg, S.; Tan, L. Z.; Tsai, H.-Z.; Kim, Y.; Lu, J.; Bradley, A. J.; Ugeda, M. M.; Meaker, K. L.; Watanabe, K.; Taniguchi, T.; Zettl, A.; Fischer, F. R.; Louie, S. G.; Crommie, M. F. ACS Nano 2014, 8, 5395.

(14) Stepanow, S.; Lingenfelder, M.; Dmitriev, A.; Spillmann, H.; Delvigne, E.; Lin, N.; Deng, X.; Cai, C.; Barth, J. V.; Kern, K. Nat. Mater. 2004, 3, 229.

(15) Marschall, M.; Reichert, J.; Weber-Bargioni, A.; Seufert, K.; Auwarter, W.; Klyatskaya, S.; Zoppellaro, G.; Ruben, M.; Barth, J. V. Nat. Chem. 2010, 2, 131.

(16) (a) Shi, Z.; Lin, N. J. Am. Chem. Soc. 2009, 131, 5376. (b) Shi, Z.; Lin, N. ChemPhysChem 2010, 11, 97.

(17) Urgel, J. I.; Ecija, D.; Auwärter, W.; Stassen, D.; Bonifazi, D.; Barth, J. V. Angew. Chem., Int. Ed. 2015, 54, 6163.

(18) Yella, A.; Lee, H.-W.; Tsao, H. N.; Yi, C.; Chandiran, A. K.; Nazeeruddin, M. K.; Diau, E. W.-G.; Yeh, C.-Y.; Zakeeruddin, S. M.; Grätzel, M. Science 2011, 334, 629.

(19) (a) Collman, J. P.; Denisevich, P.; Konai, Y. a.; Marrocco, M.; Koval, C.; Anson, F. C. J. Am. Chem. Soc. 1980, 102, 6027. (b) Guo, H.; Jiang, J.; Shi, Y.; Wang, Y.; Liu, J.; Dong, S. J. Phys. Chem. B 2004, 108, 10185.

(20) (a) Classen, T.; Fratesi, G.; Costantini, G.; Fabris, S.; Stadler, F. L.; Kim, C.; de Gironcoli, S.; Baroni, S.; Kern, K. Angew. Chem., Int. Ed. 2005, 44, 6142. (b) Surin, M.; Samorì, P.; Jouaiti, A.; Kyritsakas, N.;

Hosseini, M. W. *Angew. Chem., Int. Ed.* **2007**, *46*, 245. (c) Tait, S. L.; Langner, A.; Lin, N.; Stepanow, S.; Rajadurai, C.; Ruben, M.; Kern, K. *J. Phys. Chem. C* **2007**, *111*, 10982. (d) Skomski, D.; Tempas, C. D.; Smith, K. A.; Tait, S. L. *J. Am. Chem. Soc.* **2014**, *136*, 9862. (e) Trant, A. G.; Baddeley, C. J. *Langmuir* **2011**, *27*, 1788. (f) Langner, A.; Tait, S. L.; Lin, N.; Chandrasekar, R.; Ruben, M.; Kern, K. *Chem. Commun.* **2009**, 2502. (g) Trant, A. G.; Jones, T. E.; Baddeley, C. J. *J. Phys. Chem. C* **2007**, *111*, 10534. (h) Auwarter, W.; Ecija, D.; Klappenberger, F.; Barth, J. V. *Nat. Chem.* **2015**, *7*, 105.

(21) Heim, D.; Écija, D.; Seufert, K.; Auwärter, W.; Aurisicchio, C.; Fabbro, C.; Bonifazi, D.; Barth, J. V. *J. Am. Chem. Soc.* **2010**, *132*, 6783.

(22) (a) Bulach, V.; Hosseini, M. W. *Handbook of Porphyrin Science*; World Scientific: Singapore, 2011; Vol. 13, p 299. (b) Deiters, E.; Bulach, V.; Hosseini, M. W. *Chem. Commun.* **2005**, 3906. (c) Deiters, E.; Bulach, V.; Hosseini, M. W. *New J. Chem.* **2008**, *32*, 99. (d) Deiters, E.; Bulach, V.; Kyritsakas, N.; Hosseini, M. W. *New J. Chem.* **2005**, *29*, 1508. (e) Marets, N.; Bulach, V.; Hosseini, M. W. *New J. Chem.* **2013**, *37*, 3549. (f) Sguerra, F.; Bulach, V.; Hosseini, M. W. *Dalton Trans.* **2012**, *41*, 14683. (g) Zimmer, B.; Bulach, V.; Hosseini, M. W.; De Cian, A.; Kyritsakas, N. *Eur. J. Inorg. Chem.* **2002**, *2002*, 3079. (h) Zimmer, B.; Hutin, M.; Bulach, V.; Hosseini, M. W.; De Cian, A.; Kyritsakas, N. *New J. Chem.* **2002**, *26*, 1532.

(23) (a) Collin, J.-P.; Heitz, V.; Sauvage, J.-P. *Tetrahedron Lett.* **1991**, *32*, 5977. (b) Flamigni, L.; Collin, J.-P.; Sauvage, J.-P. *Acc. Chem. Res.* **2008**, *41*, 857. (c) Jiang, N.; Zuber, G.; Keinan, S.; Nayak, A.; Yang, W.; Therien, M. J.; Beratan, D. N. *J. Phys. Chem. C* **2012**, *116*, 9724. (d) Suzuki, M.; Uehara, T.; Arano, Y.; Hoshino, T.; Neya, S. *Tetrahedron Lett.* **2011**, *52*, 7164. (e) Uyeda, H. T.; Zhao, Y.; Wostyn, K.; Asselberghs, I.; Clays, K.; Persoons, A.; Therien, M. J. *J. Am. Chem. Soc.* **2002**, *124*, 13806.

(24) Lahaye, D.; Muthukumaran, K.; Hung, C.-H.; Gryko, D.; Rebouças, J. S.; Spasojević, I.; Batinić-Haberle, I.; Lindsey, J. S. *Bioorg. Med. Chem.* **2007**, *15*, 7066.

(25) Yu, L.; Muthukumaran, K.; Sazanovich, I. V.; Kirmaier, C.; Hindin, E.; Diers, J. R.; Boyle, P. D.; Bocian, D. F.; Holten, D.; Lindsey, J. S. *Inorg. Chem.* **2003**, *42*, 6629.

(26) Wagner, R. W.; Johnson, T. E.; Li, F.; Lindsey, J. S. *J. Org. Chem.* **1995**, *60*, 5266.

(27) LeCours, S. M.; DiMagno, S. G.; Therien, M. J. *J. Am. Chem. Soc.* **1996**, *118*, 11854.

(28) (a) Balanay, M. P.; Kim, D. H. *Phys. Chem. Chem. Phys.* **2008**, *10*, 5121. (b) Ohira, S.; Bredas, J.-L. *J. Mater. Chem.* **2009**, *19*, 7545. (c) Rintoul, L.; Harper, S. R.; Arnold, D. P. *Phys. Chem. Chem. Phys.* **2013**, *15*, 18951.

(29) Kozlowski, P. M.; Bingham, J. R.; Jarzecki, A. A. *J. Phys. Chem. A* **2008**, *112*, 12781.

(30) Barbee, J.; Kuznetsov, A. E. *Comput. Theor. Chem.* **2012**, *981*, 73.

(31) (a) Bonacchi, S.; El Garah, M.; Ciesielski, A.; Herder, M.; Conti, S.; Cecchini, M.; Hecht, S.; Samorì, P. *Angew. Chem., Int. Ed.* **2015**, *54*, 4865. (b) Haar, S.; Ciesielski, A.; Clough, J.; Yang, H. F.; Mazzaro, R.; Richard, F.; Conti, S.; Merstorf, N.; Cecchini, M.; Morandi, V.; Casiraghi, C.; Samorì, P. *Small* **2015**, *11*, 1691.

(32) (a) Ceulemans, A.; Oldenhof, W.; Gorller-Walrand, C.; Vanquickenborne, L. G. *J. Am. Chem. Soc.* **1986**, *108*, 1155. (b) Gouterman, M. *J. Chem. Phys.* **1959**, *30*, 1139. (c) Gouterman, M. *J. Mol. Spectrosc.* **1961**, *6*, 138.

(33) To investigate the lowest energy electronic configuration of the cobalt(II)-containing molecules, the cobalt complex [CoCl$_2$(terpy)py)], where terpy is 2,2′:6′,2″-terpyridine and py is pyridine, was chosen as the model core of the 2D structures and optimized at its ground state at both doublet and quartet electronic configurations. The lowest energy configuration for the doublet and the quartet possessed C_{2v} and C_s point group symmetries, respectively. The doublet configuration was computed to be 36 kJ mol^{-1} higher than the corresponding quartet.

(34) Benniston, A. C.; Harriman, A.; Pariani, C.; Sams, C. A. *Phys. Chem. Chem. Phys.* **2006**, *8*, 2051.

(35) Ciesielski, A.; Piot, L.; Samorì, P.; Jouaiti, A.; Hosseini, M. W. *Adv. Mater.* **2009**, *21*, 1131.

(36) Prendergast, K.; Spiro, T. G. *J. Am. Chem. Soc.* **1992**, *114*, 3793.

(37) Zotti, L. A.; Teobaldi, G.; Hofer, W. A.; Auwärter, W.; Weber-Bargioni, A.; Barth, J. V. *Surf. Sci.* **2007**, *601*, 2409.

(38) Fang, Z.; Liu, B. *Tetrahedron Lett.* **2008**, *49*, 2311.

(39) Hay, P. J. *J. Phys. Chem. A* **2002**, *106*, 1634.

(40) Francl, M. M.; Pietro, W. J.; Hehre, W. J.; Binkley, J. S.; Gordon, M. S.; DeFrees, D. J.; Pople, J. A. *J. Chem. Phys.* **1982**, *77*, 3654.

(41) Frisch, M. J.; Trucks, G. W.; Schlegel, H. B.; Scuseria, G. E.; Robb, M. A.; Cheeseman, J. R.; Scalmani, G.; Barone, V.; Mennucci, B.; Petersson, G. A.; Nakatsuji, H.; Caricato, M.; Li, X.; Hratchian, H. P.; Izmaylov, A. F.; Bloino, J.; Zheng, G.; Sonnenberg, J. L.; Hada, M.; Ehara, M.; Toyota, K.; Fukuda, R.; Hasegawa, J.; Ishida, M.; Nakajima, T.; Honda, Y.; Kitao, O.; Nakai, H.; Vreven, T.; Montgomery, J. A., Jr.; Peralta, J. E.; Ogliaro, F.; Bearpark, M.; Heyd, J. J.; Brothers, E.; Kudin, K. N.; Staroverov, V. N.; Kobayashi, R.; Normand, J.; Raghavachari, K.; Rendell, A.; Burant, J. C.; Iyengar, S. S.; Tomasi, J.; Cossi, M.; Rega, N.; Millam, J. M.; Klene, M.; Knox, J. E.; Cross, J. B.; Bakken, V.; Adamo, C.; Jaramillo, J.; Gomperts, R.; Stratmann, R. E.; Yazyev, O.; Austin, A. J.; Cammi, R.; Pomelli, C.; Ochterski, J. W.; Martin, R. L.; Morokuma, K.; Zakrzewski, V. G.; Voth, G. A.; Salvador, P.; Dannenberg, J. J.; Dapprich, S.; Daniels, A. D.; Farkas, Ö.; Foresman, J. B.; Ortiz, J. V.; Cioslowski, J.; Fox, D. J. *Gaussian 09*, revision D.01; Gaussian, Inc.: Wallingford, CT, 2009.